

Article

Optimization of Sensitivity of GOES-16 ABI Sea Surface Temperature by Matching Satellite Observations with L4 Analysis

Boris Petrenko ^{1,2,*}, Alexander Ignatov ¹, Yury Kihai ^{1,2} and Matthew Pennybacker ^{1,2} 

¹ NOAA STAR, NCWCP, 5830 University Research Court, College Park, MD 20740, USA; alex.ignatov@noaa.gov (A.I.); yury.kihai@noaa.gov (Y.K.); matthew.pennybacker@noaa.gov (M.P.)

² Global Science and Technology, Inc., 7855 Walker Dr # 200, Greenbelt, MD 20770, USA

* Correspondence: boris.petrenko@noaa.gov; Tel.: +1-301-683-3359, Fax: +1-301-683-3301

Received: 19 November 2018; Accepted: 17 January 2019; Published: 21 January 2019



Abstract: Monitoring of the diurnal warming cycle in sea surface temperature (SST) is one of the key tasks of the new generation geostationary sensors, the Geostationary Operational Environmental Satellite (GOES)-16/17 Advanced Baseline Imager (ABI), and the Himawari-8/9 Advanced Himawari Imager (AHI). However, such monitoring requires modifications of the conventional SST retrieval algorithms. In order to closely reproduce temporal and spatial variations in SST, the sensitivity of retrieved SST to SST_{skin} should be as close to 1 as possible. Regression algorithms trained by matching satellite observations with *in situ* SST from drifting and moored buoys do not meet this requirement. Since the geostationary sensors observe tropical regions over larger domains and under more favorable conditions than mid-to-high latitudes, the matchups are predominantly concentrated within a narrow range of *in situ* SSTs >2 85 K. As a result, the algorithms trained against *in situ* SST provide the sensitivity to SST_{skin} as low as ~0.7 on average. An alternative training method, employed in the National Oceanic and Atmospheric Administration (NOAA) Advanced Clear-Sky Processor for Oceans, matches nighttime satellite clear-sky observations with the analysis L4 SST, interpolated to the sensor's pixels. The method takes advantage of the total number of clear-sky pixels being large even at high latitudes. The operational use of this training method for ABI and AHI has increased the mean sensitivity of the global regression SST to ~0.9 without increasing regional biases. As a further development towards improved SST_{skin} retrieval, the piecewise regression SST algorithm was developed, which provides optimal sensitivity in every SST pixel. The paper describes the global and the piecewise regression algorithms trained against analysis SST and illustrates their performance with SST retrievals from the GOES-16 ABI.

Keywords: sea surface temperature; geostationary satellites; training regression SST algorithms; sensitivity to SST_{skin}; magnitude of diurnal cycle; *in situ* SST; L4 SST analysis

1. Introduction

Diurnal variations in sea surface temperature (SST) play an important role in the energy exchange between the ocean and the atmosphere (e.g., [1,2]). The key advantage of the infrared radiometers onboard the geostationary satellites is that they enable continuous monitoring of the diurnal cycle in SST (see Table 1 for list of abbreviations used in the paper). The capabilities of such monitoring have expanded with the launch of a new generation instrument, the Advanced Baseline Imager (ABI) onboard the Geostationary Operational Environmental Satellite (GOES)-16 and -17 (launched on 19 November 2016 and on 1 March 2018, respectively), and the ABI's twin sensor, the Advanced Himawari Imager (AHI) flown onboard the Japan Himawari-8 and -9 satellites (launched on

7 October 2014 and on 2 November 2016, respectively). Note that Himawari-9 is currently kept on orbit in a storage mode, pending the replacement of Himawari-8 in Japan Meteorological Agency operations, and only occasionally used as a Himawari-8 backup, when the latter is not in service.

Table 1. The list of abbreviations.

Abbreviation	Meaning
ABI	Advanced Baseline Imager
ACSPO	Advanced Clear-Sky Processor for Oceans
AHI	Advanced Himawari Imager
AVHRR	Advanced Very High Resolution Radiometer
CMC SST	Canadian Meteorological Center analysis SST
CRTM	Community Radiative Transfer Model
DCM	Magnitude of diurnal cycle
EUMETSAT	European Organization for the Exploitation of Meteorological Satellites
GFS	Global Forecast System
GOES	Geostationary Operational Environmental Satellite
GR-IS SST	Global regression SST algorithm trained against <i>in situ</i> SST
GR-L4 SST	Global regression SST algorithm trained against L4 SST
<i>i</i> Quam	<i>In situ</i> Quality Monitor
MDS	Data set of matchups
MODIS	Moderate Resolution Imaging Spectroradiometer
NLSST	Non-linear SST algorithm
NOAA	National Oceanic and Atmospheric Administration
OISST	Optimal Interpolation SST
OSTIA	Operational Sea Surface Temperature and Sea Ice Analysis SST
PWR-L4 SST	Piecewise Regression SST algorithm trained against L4 SST
SEVIRI	Spinning Enhanced Visible and Infrared Imager
S-NPP	Suomi National Polar-Orbiting Partnership
SQUAM	SST Quality Monitor
SST	Sea surface temperature
STPW	Total precipitable water vapor content along slant line of sight
TMDS-IS	Training data set of matchups of satellite observations with <i>in situ</i> SST
TMDS-L4	Training data set of matchups of satellite observations with L4 SST
VIIRS	Visible and Infrared Imager/Radiometer Suite
VZA	Satellite view zenith angle

The ABI/AHI offers five infrared atmospheric transparency window bands (centered at 3.9, 8.4, 10.3, 11.2, and 12.3 μm) suitable for SST, with high spatial resolution (2 km at nadir, which degrades to ~ 12 km at satellite view zenith angles, $VZA \sim 67^\circ$), frequent scans (every 15/10 minutes for ABI/AHI; note that NOAA also considers “Mode 6” for ABI, with a 10 minute refresh rate), and superior radiometric performance [3–5]. The NOAA Advanced Clear-Sky Processor for Oceans (ACSPO) system, initially developed to retrieve SST from polar-orbiting sensors, such as NOAA and MetOp AVHRRs; S-NPP and NOAA-20 VIIRS; and Terra and Aqua MODIS [6], was modified with the launch of Himawari-8 to process data of new generation geostationary sensors [7–9]. SSTs retrieved from GOES-16 ABI and Himawari-8 AHI reveal a clear and smooth diurnal cycle. However, accurate quantification of the diurnal cycle in SST requires modifications to the retrieval algorithms currently employed with polar-orbiting sensors.

The magnitude of the diurnal cycle (DCM) is measured as difference between the warmest daytime and the coldest nighttime SSTs. Under the conditions of strong insolation and low wind speed, the local DCM may reach several degrees Kelvin [10–12], whereas DCM averaged over larger areas (including the full observed SST domain) is typically estimated from ~ 0.3 – 0.5 K [7,13]. To correctly measure the DCM, the retrieval algorithm should be able to accurately reproduce both temporal variations and spatial contrasts in the retrieved SST. Furthermore, there may be a substantial difference between the DCM in the upper ~ 10 μm skin layer of the sea surface (T_{SKIN}), which forms the thermal infrared emission of the ocean, and T_{DEPTH} , measured at 0.2–1 m depth by drifting and moored

buoys, respectively, and customarily used for training regression SST algorithms [14,15]. This calls for algorithms more specifically targeted at T_{SKIN} versus T_{DEPTH} retrievals.

Here, we present the SST retrieval algorithms, developed in ACSPO for the ABI and AHI, to specifically improve the estimation of DCM in T_{SKIN} . The algorithms are evaluated with the emphasis on sensitivity—a scale, in which variations in true SST are reproduced in the retrieved SST, T_S [16]. It should be noted that the μ is not a measured quantity. Rather, it is calculated by replacing observed brightness temperatures with simulated derivatives of brightness temperatures in terms of SST in the regression equation and zeroing the terms independent from brightness temperatures. The radiative transfer simulations in ACSPO, including calculations of brightness temperature derivatives, are performed using the Community Radiative Transfer Model (CRTM) [17]. The input data for the CRTM are the analysis SST, produced by the Canadian Meteorological Center (CMC) [18], and atmospheric profiles of temperature and humidity from the NCEP Global Forecast System, GFS [19]. Since the CRTM treats the input SST as T_{SKIN} , the sensitivity characterizes response of T_S specifically to T_{SKIN} . We assume that errors of CRTM-based sensitivity calculations are much smaller than typical deficits in sensitivity (~ 0.1 – 0.5) for T_S retrieved from geostationary data with conventional algorithms. Optimization of sensitivity (i.e., bringing it as close to 1 as possible) is a prerequisite for accurate DCM estimation, as well as for reproduction of spatial contrasts in T_S . The importance of optimal sensitivity for the analyses of diurnal SST variations was recently stressed in, e.g., [20].

The most detailed hitherto satellite studies of the diurnal cycle [11–13,21] utilized the multiyear dataset of SST produced from the geostationary Spinning Enhanced Visible and Infrared Imager (SEVIRI) onboard METEOSAT-8 [22] with the Non-Linear SST (NLSST) algorithm [23], using two split-window bands at 10.8 and 12 μm . It was shown, however, that the SEVIRI NLSST may include significant regional biases [24] and that the sensitivity of the NLSST may be suboptimal [16,25]. Minimization of regional biases, inherent in the SEVIRI NLSST, has been the objective of developing incremental algorithms, aimed at retrieval of SST increments (i.e., “true minus first guess” SST) from brightness temperature increments (i.e., “observed minus simulated” brightness temperatures). The physical Optimal Estimation method [26] was applied to the SST retrievals from SEVIRI [24] and, recently, from Himawari-8 AHI [27]. In the algorithm [28], currently used in the reprocessing of SEVIRI data at the EUMETSAT Ocean and Sea Ice Satellite Application Facility [29], a regression equation with coefficients derived by matching absolute SSTs with absolute brightness temperatures is applied to the retrieval of SST increments from brightness temperature increments. At the early stage of preparations for the GOES-16/17 mission, the concept of the incremental regression was further elaborated [30] by deriving regression coefficients directly from SST increments matched with brightness temperature increments. Overall, the incremental algorithms were shown capable of reducing regional biases and adjusting the mean sensitivity of retrieved SST [31,32]. However, the weakness of the incremental approach is that due to a limited accuracy of the existing radiative transfer models in conjunction with the numerical weather prediction data, the incremental algorithms require correction of biases between observed and simulated brightness temperatures. The latter biases can be estimated for specific geographic regions [24,28] or as functions of certain physical variables [25,30] by averaging brightness temperature increments over prolonged time periods. As a consequence, the T_S biases are reduced in the statistical sense rather than suppressed in every single image. For this reason, we eventually decided not to implement the incremental method for AHI and ABI within ACSPO in favor of global and piecewise regression algorithms enhanced by using extended sets of radiometric bands and advanced methods of training regression coefficients.

Optimization of the T_S sensitivity has been the most challenging aspect of the adaptation of ACSPO to geostationary data. The processing of Himawari-8 AHI at NOAA started in April 2015 with the initial set of global regression coefficients produced, consistently with the polar-orbiting sensors, by the least-squares fit to *in situ* SSTs (T_{IS}) within the dataset of matchups (MDS) of clear-sky satellite brightness temperatures with T_{IS} from the NOAA *in situ* SST Quality Monitor (*iQuam*) system [33,34]. However, the sensitivity of the AHI global regression SSTs was found to be much lower than that

for the polar-orbiting sensors (VIIRS, AVHRR, and MODIS). The difference in sensitivities between geostationary and polar-orbiting sensors was due to the peculiarities of the observed SST domains. Figure 1 shows the domains observed by the SNPP VIIRS and the GOES-16 ABI. Compared to VIIRS, ABI observes mostly low-latitude regions with relatively warm SSTs, whereas the mid-to-high latitudes with colder SSTs are underrepresented in the ABI images. Moreover, those regions are observed under less favorable conditions (larger VZA and lower spatial resolution). As a result, the MDSs for geostationary sensors are dominated by matchups from low-latitude regions with relatively warm SST, resulting in a narrower distribution of matchups in terms of SST. The global regression coefficients for geostationary satellites, derived from such MDS, are mainly optimized for low-latitude regions, and the mean sensitivity of retrieved SST, averaged over the range of view zenith angles, $0^\circ \leq \text{VZA} < 67^\circ$, is as low as ~ 0.7 , compared to a typical mean sensitivity of $\sim 0.85\text{--}0.90$ for VIIRS [25].

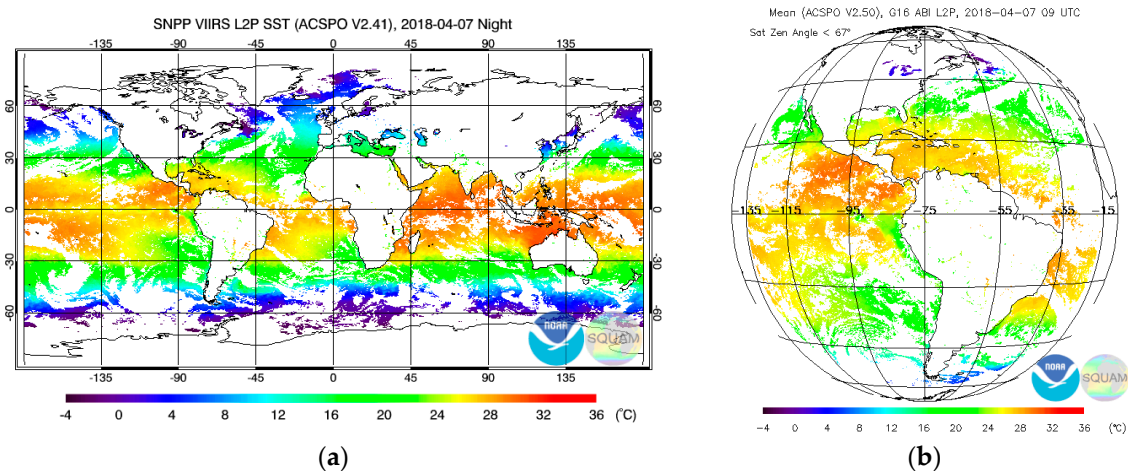


Figure 1. Composite maps of nighttime sea surface temperature (SST) retrieved with Advanced Clear-Sky Processor for Oceans (ACSPO on 4 April 2018 from (a) polar-orbiting Suomi National Polar-Orbiting Partnership Visible and Infrared Imager/Radiometer Suite (SNPP VIIRS) and (b) GOES-16 Advanced Baseline Imager (ABI) (the latter taken at 9:00 UTC). Both images are from the NOAA SST Quality Monitor (NOAA SQUAM) [35,36].

In order to increase the sensitivity of the global regression SST, the Constrained Least-Squares Method for training regression coefficients was tested, which fits T_{IS} under a predefined value of mean sensitivity over the MDS [8]. This way, the mean sensitivity of AHI global regression SST was raised to ~ 0.95 , which, however, came at the expense of larger regional T_S biases. An alternative method for training the regression coefficients, based on matching nighttime satellite observations with CMC analysis of SST, has been explored after ABI thermal IR data became available in January 2017. Note that the CMC SST is a foundation level 4 product, derived on a daily basis on a 0.1° grid from nighttime satellite SSTs and anchored to *in situ* SST measurements [18]. ACSPO interpolates the gridded CMC SST to every pixel of the sensor. The advantage of the newly developed training method is that, in contrast with matchups with *in situ* SST, the number of clear-sky pixels, supplied with CMC SST, is much larger than the number of matchups with *in situ* SST, even in near-polar regions. Using the regression coefficients, calculated with the least-squares method from matchups with CMC SST, the mean sensitivity of the global regression SST was raised to ~ 0.9 , without a noticeable increase in regional biases. The next step towards optimization of T_{SKIN} estimates has been the development of the piecewise regression algorithm, which provides optimal and uniform sensitivity in each SST pixel. In this paper, we compare the performance of the global regression algorithms trained against *in situ* and CMC SSTs (GR-IS SST and GR-L4 SST, respectively), and explore the potential of further sensitivity optimization by employing a PWR algorithm, trained against the CMC (PWR-L4).

2. Regression SST Equation

ACSP0 derives SST from four longwave IR ABI/AHI bands centered at 8.4, 10.3, 11.2, and 12.3 μm , within the range $0^\circ < \text{VZA} < 67^\circ$. The shortwave band, centered at 3.9 μm , is currently not used because during the day it is affected by the reflected solar radiation, and using it at night only might introduce a discontinuity in the observed diurnal signal. The four-band SST equation takes the following form:

$$T_S = a + \mathbf{C}^T \mathbf{R}. \quad (1)$$

Here, \mathbf{R} is a vector of regressors:

$$\mathbf{R}^T = \{T_{11}, (T_{11} - T_8), (T_{11} - T_{10}), (T_{11} - T_{12}), T_{11} S_\theta, (T_{11} - T_8) S_\theta, (T_{11} - T_{10}) S_\theta, (T_{11} - T_{12}) S_\theta, \\ (T_{11} - T_8) T_S^0, (T_{11} - T_{10}) T_S^0, (T_{11} - T_{12}) T_S^0, S_\theta\}; \quad (2)$$

\mathbf{C} is a vector of regression coefficients; a is offset; T_8 , T_{10} , T_{11} , and T_{12} are brightness temperatures observed in the 8.4, 10.3, 11.2, and 12.3 μm bands, respectively; $S_\theta = 1/\cos(\theta) - 1$; θ is VZA; T_S^0 is the CMC SST (in $^\circ\text{C}$), interpolated from the original 0.1° grid to sensor's pixels. Derivatives of brightness temperatures in terms of SST, D_8 , D_{10} , D_{11} , and D_{12} , are calculated with the CRTM, and sensitivity in every SST pixel is calculated as follows:

$$\mu(\mathbf{K}, \mathbf{C}) = \mathbf{C}^T \mathbf{K}, \quad (3)$$

$$\mathbf{K}^T = \{D_{11}, (D_{11} - D_8), (D_{11} - D_{10}), (D_{11} - D_{12}), D_{11} S_\theta, (D_{11} - D_8) S_\theta, (D_{11} - D_{10}) S_\theta, (D_{11} - D_{12}) S_\theta, \\ (D_{11} - D_8) T_S^0, (D_{11} - D_{10}) T_S^0, (D_{11} - D_{12}) T_S^0, 0\} \quad (4)$$

The extended set of regressors in Equation (2) enables efficient fitting of matched SST (i.e., T_{IS} in GR-IS SST or T_S^0 in GR-L4 SST and PWR-L4 SST) within the corresponding MDSs. The method for stable estimation of regression coefficients [8] minimizes/avoids potential instabilities, caused by correlations between the regressors within the MDS with minimum loss of the information.

3. Training Global Regression Algorithms

The dataset of matchups with *in situ* SST (MDS-IS), used in this study, includes $N = 977,439$ matchups of ABI clear-sky observations (both day and night) with high-quality *iQuam* drifting and moored buoys. The matchups were collected from April 2017 to March 2018, with a time/space window of 15 min and 10 km, respectively. Every matchup was supplied with simulated brightness temperature derivatives in terms of SST, required for sensitivity calculations, and with GFS data, including wind speed near the sea surface, V , and total column precipitable water vapor content in the atmosphere, W . The difficulty of using *in situ* SST in the context of T_{SKIN} retrievals is that T_{IS} represents T_{DEPTH} , which may significantly deviate from T_{SKIN} . The discrepancy between T_{SKIN} and T_{IS} reaches the maximum during the daytime under the conditions of strong insolation and low wind speeds near the sea surface [14,15]. To minimize the effect of this discrepancy on trained GR-IS SST coefficients, the daytime matchups with $V < 6$ m/s were excluded from the training MDS (TMDS-IS). This has reduced the number of matchups within the TMDS-IS to $N = 795,877$ matchups, or by 18.6%.

The dataset used for training the GR-L4 SST and the PWR-L4 coefficients (TMDS-L4) was composed from nighttime clear-sky ABI L2P SST pixels, supplied with CMC SSTs. Only nighttime data were used because the foundation CMC SST is produced from nighttime SST data (for which the foundation SST is most close to T_{SKIN}) and does not capture the daytime variations in T_{SKIN} . Therefore, using daytime SST pixels for training the GR-L4 SST coefficients would result in additional errors. The TMDS-L4 was formed from 744 ABI images taken every hour from 15 December 2017 to 15 January 2018. A full ABI L2P SST image contains on average 3.2×10^6 clear-sky pixels, with approximately half of those being nighttime. The total number of nighttime pixels within the TMDS-L4 reaches 1.19×10^9 , which is 1.5×10^3 times larger than the number of matchups within the TMDS-IS.

The large number of pixels within the TMDS-L4 allows improvement to the performance of the GR-L4 SST compared with the GR-IS SST. Curves 1 and 2 in Figure 2 show the normalized histograms of matchups within TMDS-IS and TMDS-L4, as functions of CMC SST. For both these distributions the majority of matchups is concentrated at warm SSTs > 285 K, and the histogram for TMDS-L4 is even narrower than for TMDS-IS. The advantage of TMDS-L4, however, is that the absolute number of clear-sky pixels in the high-latitude regions is much larger than the number of matchups with *in situ* SST. It is possible, therefore, to improve the performance of the GR-L4 SST by accounting for the pixels from the under-represented regions with larger weights. When training the GR-L4 SST and the PWR-L4 SST algorithms, the weights of the pixels within each $5^\circ \times 5^\circ$ lat/lon box were selected in inverse proportion to total numbers of clear-sky pixels within the box. The curve 3 in Figure 2 shows the modified normalized histogram, which accounts for weights of the clear-sky pixels within the TMDS-L4. The weighting expands the histogram and increases the contribution of cold pixels to the overall statistics.

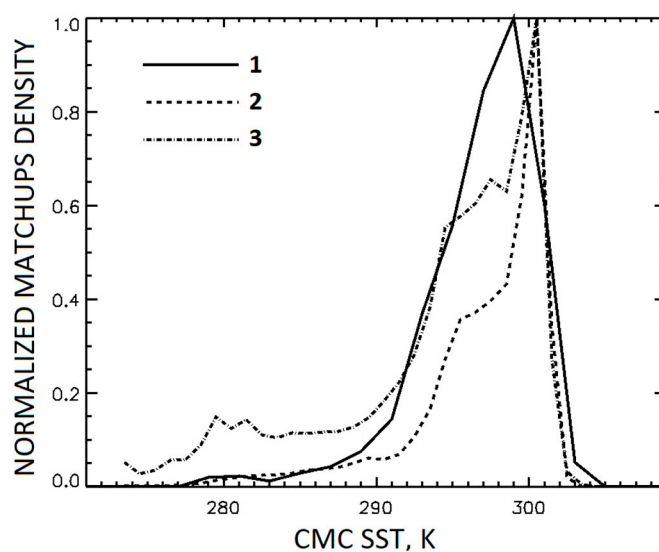


Figure 2. Normalized histograms of matchups within (1) training data set of matchups of satellite observations with *in situ* SST (TMDS-IS) ($N = 795,877$) (2) TMDS-L4 ($N = 1.19 \times 10^9$), (3) same as (2) but taking into account weights of the pixels within the MDS-L4 (as explained in Section 3). All histograms are shown as functions of Canadian Meteorological Center (CMC) SST.

The GR-IS SST algorithm was trained with the least-squares method, which minimizes the global standard deviation of T_S from T_{IS} . The GR-L4 SST was trained by minimization of the weighted standard deviation of T_S from T_S^0 . After training, the offsets of the GR-IS and GR-L4 equations were adjusted to zero bias between retrieved SSTs and T_{IS} averaged over matchups within the TMDS-IS from 12 am to 7 am local solar time.

4. The PWR-L4 SST Algorithm

As will be shown in Section 5, the GR-L4 SST increases the sensitivity compared with the GR-IS SST but leaves it suboptimal and non-uniform. The goal of the PWR-L4 SST is to further optimize the sensitivity in every pixel. The algorithm is constructed and performs as follows.

During off-line training, the vector of GR-L4 coefficients, \mathbf{C}_{GR-L4} , is derived from TMDS-L4, as described in Section 3, and the GR-L4 sensitivity, $\mu_{GR-L4} = \mathbf{C}_{GR-L4}^T \mathbf{K}$, is calculated for all pixels (\mathbf{K} is defined in Equation (4)). The whole TMDS-L4 is subdivided into 9 subsets in terms of μ_{GR-L4} :

$$I = 1: \mu_{GR-L4} < 0.6 \quad (5a)$$

$$I = 2, 3, \dots, 8: 0.6 + 0.05(I - 2) \leq \mu_{GR-L4} < 0.6 + 0.05(I - 1) \quad (5b)$$

$$I = 9: \mu_{GR-L4} \geq 0.95 \quad (5c)$$

Here, i is the number of the subset. The first guess of the PWR-L4 coefficients for the i^{th} subset, \mathbf{C}_1^i , is derived with the Constrained Least-Squares Method [8], by minimization of the weighted standard deviation of $T_S - T_S^0$ under the constraint on the mean sensitivity: $(\mathbf{C}_1^i)^T \langle \mathbf{K} \rangle = 1$, $\langle * \rangle$ denotes averaging over the pixels belonging to a given TMDS-L4 subset. The offsets a^i are defined in order to zero the bias of T_S with respect to *in situ* SST over the subset of TMDS-IS, which includes matchups with the corresponding sensitivities, taken from 0 to 7 am of the local solar time:

$$a_1^i = \langle \langle T_{IS} \rangle \rangle - (\mathbf{C}_1^i)^T \langle \langle \mathbf{R} \rangle \rangle \quad (6)$$

$\langle \langle * \rangle \rangle$ in Equation (6) denotes averaging over a given TMDS-IS subset. Similarly, the particular offsets of the GR-L4 SST equations for the i^{th} subset, b^i , are defined as

$$b^i = \langle \langle T_{IS} \rangle \rangle - (\mathbf{C}_{GR-L4}^i)^T \langle \langle \mathbf{R} \rangle \rangle^i + b_0 \quad (7)$$

The values of \mathbf{C}_1^i , a_1^i , b^i and mean values of the GR-L4 SST sensitivities, $\mu^i = \langle \mu_{GR-L4} \rangle$, $I = 1, 2, \dots, 9$, are stored in the look-up table.

During processing, every SST pixel is attributed to a specific subset depending on a pixel value of μ_{GR-L4} and the PWR-L4 SST equation for this pixel is modified with two sequential iterations. The second iteration of the PWR-L4 coefficients and the offsets, $\{a_2, \mathbf{C}_2\}$ ensures their continuity in terms of μ_{GR-L4} :

If $\mu_{GR-L4} \leq \mu_1$:

$$\mathbf{C}_2 = \mathbf{C}_1^1, a_2 = a_2^1 \quad (8)$$

If $\mu_i < \mu_{GR-L4} \leq \mu_{i+1}$, $I = 1, 2, \dots, 8$:

$$\mathbf{C}_2 = \mathbf{C}_1^i + [(\mathbf{C}_1^{i+1} - \mathbf{C}_1^i) / (\mu^{i+1} - \mu^i)] (\mu_{GR-L4} - \mu^i), a_2 = a_2^i + [(a_2^{i+1} - a_2^i) / (\mu^{i+1} - \mu^i)] (\mu_{GR-L4} - \mu^i) \quad (9)$$

If $\mu_{GR-L4} > \mu_9$:

$$\mathbf{C}_2 = \mathbf{C}_1^9, a_2 = a_2^9 \quad (10)$$

The third iteration brings the PWR-L4 sensitivity exactly to 1 by extrapolation/interpolation between the second iteration of the PWR-L4 sensitivities, $\mu_2 = \mathbf{C}_2^T \mathbf{K}$, and μ_{GR-L4} :

$$\mathbf{C}_3 = \mathbf{C}_{GR-L4} + [(\mathbf{C}_2 - \mathbf{C}_{GR-L4}) / (\mu_2 - \mu_{GR-L4})] (1 - \mu_{GR-L4}), a_3 = b^i + \{(a_2 - b^i) / [\mu_2 - \mu_{GR-L4}]\} (1 - \mu_{GR-L4}) \quad (11)$$

Considering that $\mu_{GR-L4} = \mathbf{C}_{GR-L4}^T \mathbf{K}$, the sensitivity of the T_S , produced with coefficients \mathbf{C}_3 from Equation (11), $\mathbf{C}_3^T \mathbf{K} \equiv 1$. Finally, the PWR-L4 SST is calculated as

$$T_S = a_3 + \mathbf{C}_3^T \mathbf{R} \quad (12)$$

5. Validation Against *In Situ* SST

In this Section, the explored algorithms are evaluated and compared using matchups from the MDS-IS. In order to minimize the contribution of the discrepancies between T_{IS} and T_{SKIN} to the validation statistics, biases and standard deviations of $T_S - T_{IS}$, as well as mean sensitivities are calculated from TMDS-IS, which, as described in Section 3, excludes daytime matchups with GFS wind speeds $V < 6$ m/s. In contrast, the DCM estimates are produced from the full MDS-IS, taking into account both daytime and nighttime matchups at all wind speeds. It should be noted that since the TMDS-IS was used for training the GR-IS coefficients, it can be viewed as a dependent MDS in terms of validating the GR-IS SST. However, it is independent in terms of validating the GR-L4 and the

PWR-L4 SSTs. This suggests that the conditions of the comparison are more favorable for the GR-IS SST than for two other algorithms.

Absorption by the atmospheric water vapor is a major factor, modifying the responses of brightness temperatures, observed in the atmospheric transmission window, to variations in SST (e.g., [37,38]). The performance of the regression algorithms (including sensitivity) usually degrades with the increase of the water vapor content along the sensor's slant line of sight, $STPW = W \times \sec(\theta)$ [25]. It is important, therefore, to determine the ranges of STPW, suitable for retrieval of T_{SKIN} with the explored algorithms. The statistical factor which should also be considered when comparing different training techniques is the distribution of matchups within the training MDS. Figure 3 shows the normalized histograms of matchups within TMDS-IS and TMDS-L4 as functions of STPW. The histogram for TMDS-L4 accounts for weighting the pixels during training the GR-L4 and PWR-L4 coefficients, as described in Section 3. The latter histogram shows wider maximum and increased contribution of matchups with $STPW < 30 \text{ kg/m}^2$, typical for mid- and high latitudes. Figure 4 shows mean sensitivities, biases, and standard deviations as functions of STPW. All algorithms perform best near the maxima of the corresponding matchups' distributions at $30 < STPW < 50 \text{ kg/m}^2$, rather than at the minimum of STPW, as one could expect from physical considerations. At smaller STPWs the biases and the standard deviations increase for all three algorithms, and the sensitivities for the GR-IS and GR-L4 SSTs reduce due to reduced relative numbers of corresponding matchups within the training MDSs. At larger STPWs, the statistics are affected by a combination of increasing atmospheric absorption and decreasing relative numbers of matchups. In Figure 4a, the GR-IS SST sensitivity is as low as 0.75 at its maximum near $STPW = 30 \text{ kg/m}^2$ and reduces to 0.40 at $STPW = 130 \text{ kg/m}^2$. The sensitivity of the GR-L4 SST reaches 0.95 at $STPW = 20 \text{ kg/m}^2$ but reduces to 0.56 at $STPW = 130 \text{ kg/m}^2$. The sensitivity of the PWR-L4 SST, by design, remains constant and optimal at all STPWs. In Figure 4b, the biases for all three SSTs do not exceed 0.1 K within the range $20 < STPW < 80 \text{ kg/m}^2$. At $STPW < 20 \text{ kg/m}^2$, the large bias in the GR-IS SST is caused by the insufficient number of matchups within the TMDS-IS, whereas the biases in the GR-L4 SST and, especially, PWR-L4 SST increase to a lesser extent. In Figure 4c, the standard deviations for all three SSTs increase with $STPW > 40 \text{ kg/m}^2$, consistently with the sensitivities in Figure 4a. Thus, we conclude that the sensitivity of the GR-L4 SST is suboptimal for estimations of the DCM in T_{SKIN} within the whole range of STPW. The DCM estimates from GR-L4 SST may be appropriate at $STPW < 60 \text{ kg/m}^2$ but become suboptimal at larger STPWs because of degraded sensitivity. On the other hand, the T_{SKIN} retrievals and DCM estimates, made from the PWR-L4 SST, may be inefficient at large STPWs due to degraded accuracy and precision. Considering the above, we restrict the range of STPW for T_{SKIN} retrieval with $STPW < 100 \text{ kg/m}^2$. This excludes nearly 0.6% of the MDS-IS and TMDS-IS matchups from the further analysis.

Figure 5a illustrates the effect of sensitivity on the reproduction of the diurnal cycle in T_S with three algorithms by showing the hourly biases of $T_S - T_S^0$ as functions of local solar time. The latter biases were estimated from the MDS-IS, using 970,371 daytime and nighttime matchups at all wind speeds and with $STPW < 100 \text{ kg/m}^2$. Figure 5a also shows the hourly biases in $T_{IS} - T_S^0$. The diurnal cycles are well expressed in all three retrieved SST as well as in T_{is} , although with substantially different DCMs. The maxima and the minima in $T_{IS} - T_S^0$ take place later than in $T_S - T_S^0$, consistent with the fact that the "skin" layer cools down and warms up faster than the "depth" layer, at which the *in situ* SST is measured. Figure 5b shows the hourly biases in $T_S - T_{IS}$. The biases in $T_S - T_{IS}$ in Figure 5b are smaller than in $T_S - T_S^0$ in Figure 5a. One can also notice that the maxima and the minima of biases in $T_S - T_{IS}$ shift to a later time when the mean sensitivity of an SST product increases.

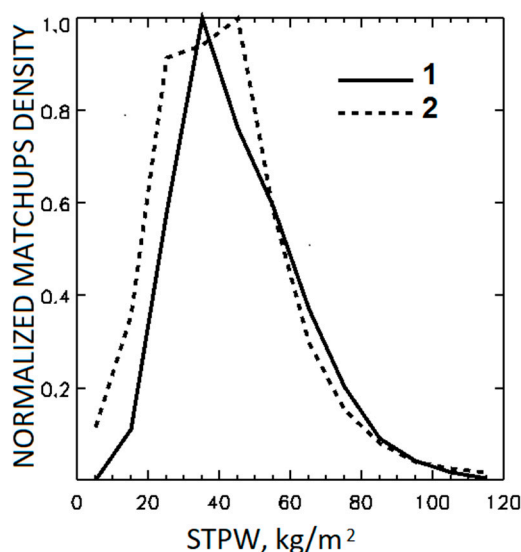


Figure 3. Normalized histograms in terms of total precipitable water vapor content along slant line of sight (STPW) of (1) matchups with *in situ* SSTs within TMDS-IS and (2) weighted matchups of nighttime ABI pixels with CMC L4 SSTs within the MDS-L4.

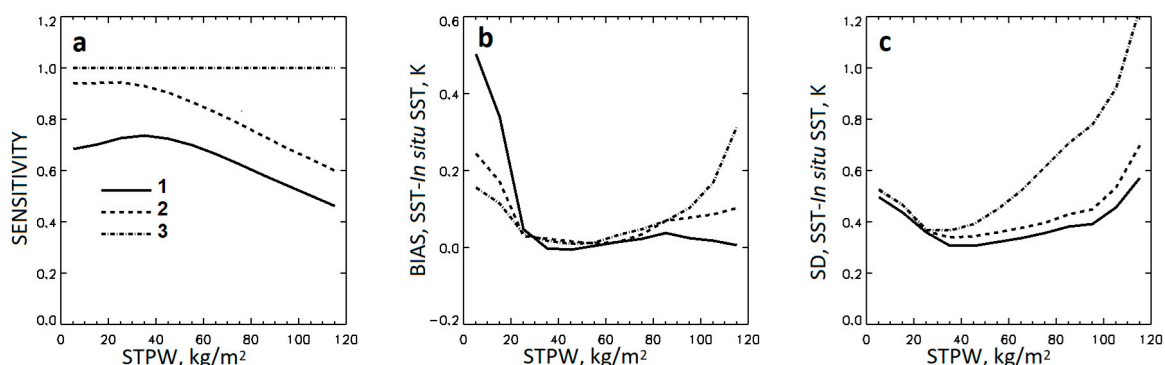


Figure 4. (a) Sensitivity, (b) bias and (c) standard deviation with respect to *in situ* SST of the (1) GR-IS SST, (2) GR-L4 SST, and (3) PWR-L4 SST. All shown as functions of slant-path total precipitable water vapor content, STPW.

Table 2 summarizes mean sensitivities, SDs, and DCMs, estimated from the corresponding subsets of matchups. Overall, training the GR coefficients against CMC increases all three statistics compared with training against *in situ* SST and so does the adjustment of sensitivity in the PWR-L4 SST. More specifically, the 25% increase in mean sensitivity between the GR-IS SST and the GR-L4 SST results in comparable (22%) increase in DCM and disproportionally small (9%) increase in SD. On the other hand, the 11% increase in mean sensitivity between the GR-L4 and PWR-L4 SSTs causes a 12% increase in DCM and a larger (14%) increase in SD. This result, consistent with Figure 4b,c, suggests that estimation of the PWR-L4 coefficients with the CLS method may cause amplification of regional biases compared with those in the GR-L4 SST.

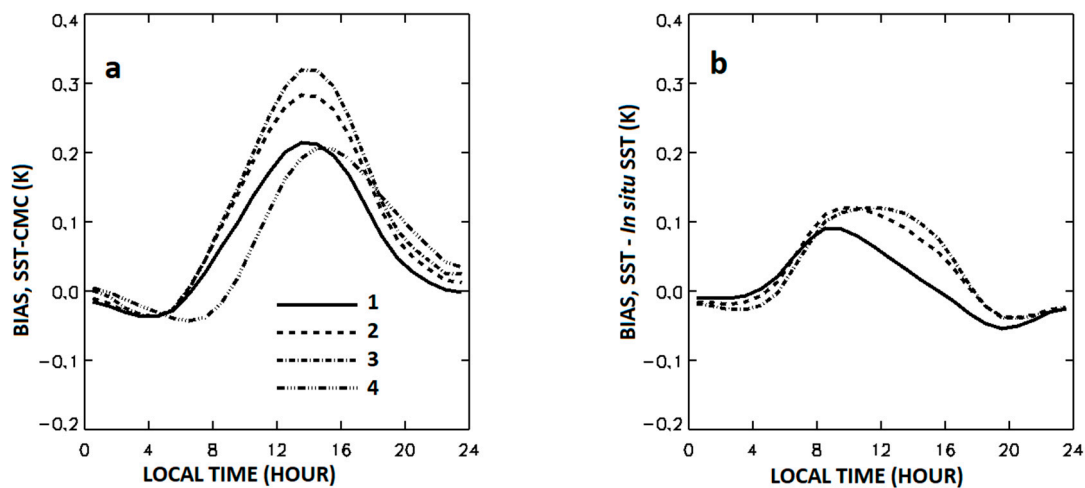


Figure 5. (a) Diurnal cycles in $T_S - T_S^0$ averaged over the full ABI MDS-IS (April 2017–March 2018) for (1) GR-IS SST (2) GR-L4 SST, (3) PWR-L4 SST and (4) *in situ* SST. (b) Diurnal mean deviations of (1) GR-IS SST (2) GR-L4 SST and (3) PWR-L4 SST from *in situ* SST. All shown as functions of local solar time.

Table 2. Mean sensitivities, standard deviations of retrieved SST – *in situ* SST, and average magnitudes of diurnal cycle (DCMs), estimated from MDS-IS, using matchups with STPW < 100 kg/m².

Algorithm	Mean Sensitivity	Standard Deviation	DCM
GR-IS SST	0.72	0.32 K	0.27 K
GR-L4 SST	0.90	0.35 K	0.33 K
PWR-L4 SST	1.00	0.40 K	0.37 K

6. Processing GOES-16 ABI Data

The three algorithms have been implemented within the experimental version of ACSPO and tested on GOES-16 ABI data from 1 March–31 March 2018. Since the operational ACSPO Clear-Sky mask [39] uses retrieved SST as one of the clear-sky predictors, the clear-sky SST domains may be somewhat different for different retrieval algorithms. To ensure the comparison of the algorithms on the same domain, a single clear-sky mask, generated with the GR-L4 SST, was consistently employed with all three algorithms. Figure 6 shows geographical distributions of sensitivities for three SSTs retrieved from the ABI data on 1 March 2018 at 20:00 UTC (close to the maximum of the diurnal warming signal within the GOES-16 ABI domain). Figure 7 shows deviations of the retrieved SSTs from CMC SST for the same ABI data. The statistics of sensitivities for the images in Figure 6 and of $T_S - T_S^0$ for the images in Figure 7 are given in Table 3. In Figure 6, the GR-IS SST has the lowest and variable sensitivity. The GR-L4 SST sensitivity is higher than for the GR-IS SST and is also variable. For both the GR-IS SST and the GR-L4 SST, the sensitivities are especially low in the low latitudes at large VZAs, due to large atmospheric absorption along the line of sight, consistent with the behavior of sensitivities at large STPWs in Figure 4a. The GR-IS sensitivity is also reduced in the near-polar zones, which are poorly represented within TMDS-IS. The PWR-L4 SST, by design, provides optimal and uniform sensitivity, $\mu \equiv 1$, over the full SST domain.

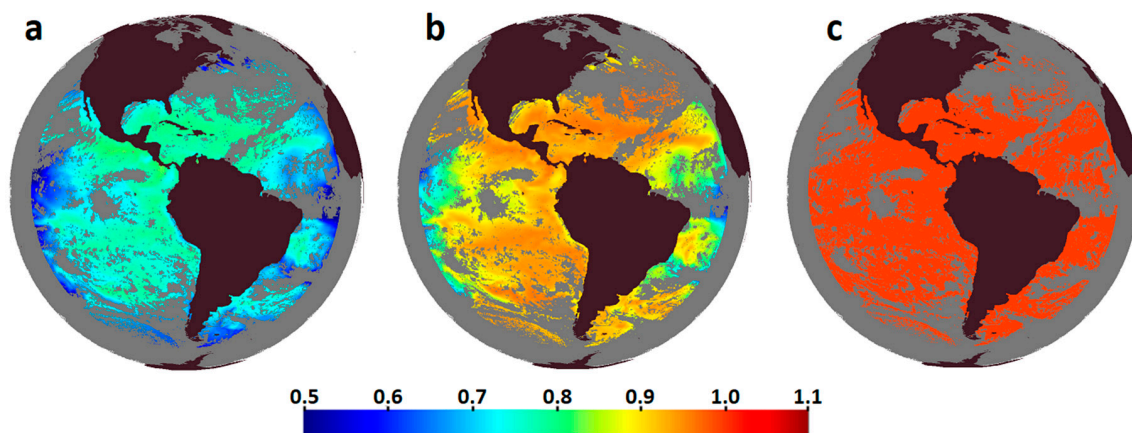


Figure 6. Images of the sensitivity of GOES-16 ABI SST for (a) GR-IS SST, (b) GR-L4 SST, and (c) PWR-L4 SST at 20:00 UTC 1 March 2018.

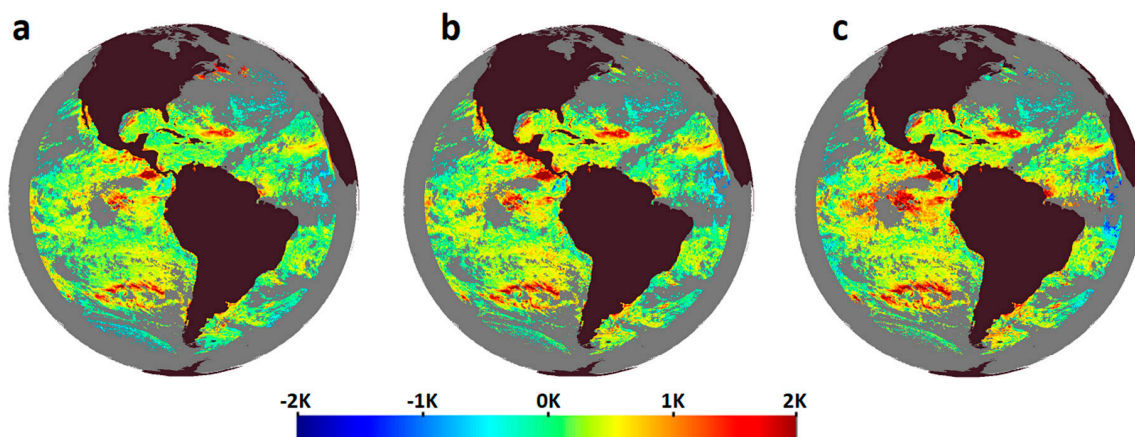


Figure 7. Images of the deviation of GOES-16 ABI SST from CMC for (a) GR-IS SST, (b) GR-L4 SST, and (c) PWR-L4 SST at 20:00 UTC 1 March 2018.

Table 3. Statistics of sensitivities and deviations of ABI SST from CMC SST corresponding to the images in Figures 6 and 7.

Algorithm	Mean Sensitivity	Standard Deviation	DCM
GR-IS SST	0.72	0.32 K	0.27 K
GR-L4 SST	0.90	0.35 K	0.33 K
PWR-L4 SST	1.00	0.40 K	0.37 K

Overall, the three products show similar diurnal warming patterns, but with different amplitudes. The exceptions are unrealistically warm biases in the GR-IS SST in the North Atlantic Ocean and smaller biases at the south-western edge of the image, which are not reproduced (or are less noticeable) in the two other SSTs. Differences between the GR-L4 and the PWR-L4 SSTs are more noticeable in regions with relatively low GR-L4 sensitivities: for instance, the PWR-L4 SST is warmer in the Equatorial Pacific Ocean and in the Southern Atlantic and colder in the Equatorial Atlantic at the eastern edge of the image, due to the effect of the Saharan dust outbreak.

Figure 8 shows the time series of biases in retrieved SST–CMC SST for 20–30 March 2018. The DCMs increase from GR-IS to GR-L4 and to PWR-L4 SST. Table 4 shows the mean sensitivities and DCMs for three algorithms averaged over the month from 1–31 March 2018. The DCMs in Table 4 are roughly proportional to mean sensitivities.

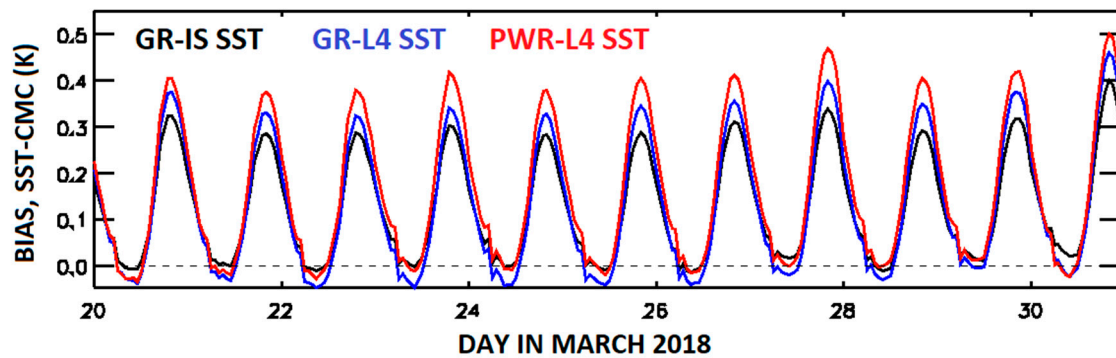


Figure 8. Time series of the bias of $T_S - T_S^0$ derived from GR-IS SST, GR-L4 SST, and PWR-L4 SST for 24–30 March 2018.

Table 4. Mean sensitivities and magnitudes of the diurnal cycle, averaged from 1 to 31 March 2018, for the three explored algorithms.

Algorithm	Mean Sensitivity	DCM
GR-IS SST	0.73	0.34 K
GR-L4 SST	0.91	0.43 K
PWR-L4 SST	1.00	0.47 K

Figure 9 shows the mean values of DCMs, averaged from 1–31 March 2018, as functions of STPW. The corresponding dependencies for sensitivities are similar to those produced from matchups and shown in Figure 4a. The unrealistically large DCM in the GR-IS SST at $STPW < 10 \text{ kg/m}^2$ confirms that this algorithm is inefficient at small STPWs. Other than that, the changes in DCM between the algorithms are consistent with the differences in the sensitivities. The difference between the DCMs estimated from the GR-IS SST and the GR-L4 SST is the largest at $STPW < 60 \text{ kg/m}^2$. In contrast, the difference between the DCMs for GR-L4 SST and PWR-L4 SST is small at $10 < STPW < 40 \text{ kg/m}^2$ and increases with STPW growing over 40 kg/m^2 due to increased difference in sensitivities. Assuming that the maximum of the clear-sky pixels distribution takes place at $30 < STPW < 50 \text{ kg/m}^2$, consistent with the maximum of the distribution of matchups in Figure 3, the adjustment of the DCM estimates in the PWR-L4 SST at larger STPWs may essentially exceed the mean difference between the average DCM values for GR-L4 and PWR-L4 SSTs shown in Table 4.

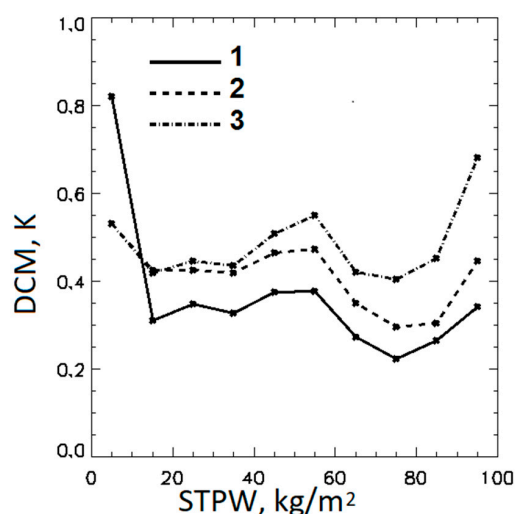


Figure 9. Mean DCMs for (1) GR-IS SST, (2) GR-L4 SST, and (4) PWR-L4 SST, averaged from 1 to 31 March 2018, as functions of STPW.

7. Training SST Algorithms Against Different L4 Analyses

L4 SST analyses, available from different producers, are not identical and may report different SST values for the same time and geographical regions. Table 5 illustrates this statement by showing biases and standard deviations between the CMC SST and the Operational Sea Surface Temperature and Sea Ice Analysis (OSTIA) [40] as well as between CMC and the Optimal Interpolation SST (OISST) [41]. The statistics were produced for 31 December 2017 by averaging over the ABI SST domain within the range of VZAs from 0 to 67°. In both cases the standard deviations between the compared L4 analyses are significant. The difference between CMC and OISST is larger than between CMC and OSTIA in terms of both bias and standard deviation, and may be considered as an extreme case. In this Section, we evaluate possible variations in T_S retrieved with the GR-L4 and the PWR-L4 algorithms, which may be caused by training against different SST analyses.

Table 5. Bias and standard deviation of the differences between L4 analyses for 31 December 2017.

Compared L4 SSTs	Bias	Standard Deviation
CMC vs OSTIA	0.01 K	0.22 K
CMC vs OISST	−0.07 K	0.36 K

Table 6 shows the statistics, averaged over the clear-sky GOES-16 ABI SST domain, for the difference in T_S caused by training the same algorithm against different L4 analyses (i.e., CMC vs. OSTIA or CMC vs. OISST). In all cases, the algorithms were trained using ABI and L4 SST data from 15 December 2017 to 15 January 2018. The training procedures were similar to those described in Sections 3 and 4 with the exception that the offsets of the SST equations were selected to fit the nighttime L4 SST rather than *in situ* SSTs. The statistics are shown for two ABI images taken on 31 December 2017 at 9:00 and 20:00 UTC, close, respectively, to the minimum and the maximum of the diurnal cycle in the GOES-16 ABI SST domain. The difference between the daytime and nighttime biases caused by training against different L4 analyses is negligible in all cases. This suggests that the estimates of DCM, averaged over the full ABI SST domain, are practically insensitive to the selection of the L4 analysis for training. The standard deviations of variations in the GR-L4 SST, do not exceed 0.06 K. The corresponding standard deviations for the PWR-L4 SST are larger, especially in the case of switching between CMC and OISST. This suggests that the PWR-L4 SST algorithm requires more careful selection of the analysis SST for training.

Table 6. Bias and standard deviation of variations in the GR-L4 SST and the PWR-L4 SSTs caused by training on different L4 analyses, averaged over the GOES-16 ABI clear-sky SST domains on 31 December 2017 at 9:00 and 20:00 UTC.

Compared L4 SSTs	Night (9:00 UTC)		Day (20:00 UTC)	
	Bias	Standard Deviation	Bias	Standard Deviation
	GR-L4 SST			
CMC vs OSTIA	−0.02 K	0.02 K	−0.02 K	0.02 K
CMC vs OISST	−0.02 K	0.06 K	−0.02 K	0.06 K
	PWR-L4 SST			
CMC vs OSTIA	0.02 K	0.08 K	0.02 K	0.07 K
CMC vs OISST	0.00 K	0.13 K	0.01 K	0.13 K

8. Summary and Conclusions

The sensitivity of retrieved SST to T_{SKIN} is a characteristic of an SST retrieval algorithm, which determines the reproduction of true spatial and temporal SST variations in retrieved SST. The sensitivity directly affects the magnitude of diurnal SST variations, estimated from geostationary sensors, and, therefore, it is of particular importance for the quantitative monitoring of the diurnal cycle in SST.

The sensitivity may substantially vary for different SST algorithms depending on the algorithm's design and the method of training regression coefficients. Optimization of the sensitivity at the stage of algorithm development, i.e., bringing it as close to 1 as possible, is a prerequisite for accurate estimation of the magnitude of the diurnal cycle in SST.

The conventional method of training regression SST algorithms, developed earlier for polar-orbiting sensors, implies matching satellite observations with drifting and moored buoys. We have found this method suboptimal for geostationary sensors because it provides the sensitivity to T_{SKIN} , averaged over the full observed SST domain, as low as ~ 0.7 . As an alternative to training against *in situ* SST, we have developed the method of training by matching nighttime clear-sky satellite observations with analysis L4 SST in conjunction with weighting the clear-sky pixels in the inverse proportion to their spatial density. With the newly developed training method, the average sensitivity of the global regression SST for GOES-16 ABI has been increased from ~ 0.7 to ~ 0.9 without noticeable increase of regional biases. However, even with this improved training method, the sensitivity of the global regression SST remains variable and suboptimal.

The ultimate optimization of sensitivity has been further accomplished with the development of the piecewise regression algorithm, which exploits the segmentation of the SST domain in terms of sensitivity of the global regression SST, trained against L4 CMC SST, and calculates the coefficients for each segment under the mean sensitivity constrained at 1. While the improvement in sensitivity of the global regression algorithm due to training against L4 SST increases the magnitude of the diurnal cycle in SST almost uniformly over the ABI SST domain, the piecewise regression SST algorithm further increases the magnitude of the diurnal cycle in the areas with larger atmospheric absorptions, in which the sensitivity of the global regression SST is relatively low.

The global regression algorithm with coefficients, trained on CMC SST, has been implemented as a primary ACSPO algorithm for GOES-16/17 ABI and Himawari-8 AHI, starting with the operational ACSPO version 2.60. The PWR "skin" algorithm has been implemented as an experimental algorithm in ACSPO version 2.61 for internal testing. The future work will be focused on detailed validation of T_{SKIN} retrievals from the aforementioned satellites and optimization of SST retrieval algorithms, including minimization of the diurnal variability of biases in retrieved SST.

Author Contributions: Conceptualization: B.P. and A.I.; Methodology: B.P.; Software: B.P., Y.K. and M.P.; Validation: B.P.; Formal Analysis: B.P.; Investigation: B.P.; Resources: A.I.; Data Curation: B.P., Y.K. and M.P.; Writing-Original Draft Preparation: B.P.; Writing-Review and Editing: B.P., A.I. and M.P.; Visualization: B.P.; Supervision: A.I.; Project Administration: A.I.; Funding Acquisition: A.I.

Funding: This work was funded by the US GOES-R and NOAA ORS Programs.

Acknowledgments: We thank GOES-R Director Pam Sullivan and STAR Lead Jaime Daniels, and ORS Managers, Paul DiGiacomo and Marilyn Yuen-Murphy, for support. Thanks also go to our NOAA colleagues Maxim Kramar, Xinjia Zhou, Olafur Jonasson, Irina Gladkova, and John Sapper, for helpful discussions and help. The views, opinions, and findings contained in this paper are those of the authors and should not be construed as an official NOAA or US Government position, policy, or decision.

Conflicts of Interest: The authors declare no conflict of interest.

References

1. Kawai, Y.; Wada, A. Diurnal sea surface temperature variation and its impact on the atmosphere and ocean: A review. *J. Oceanogr.* **2007**, *63*, 721. [[CrossRef](#)]
2. Clayson, C.A.; Bogdanoff, A.S. The effect of diurnal sea surface temperature warming on climatological air-sea fluxes. *J. Clim.* **2013**, *26*, 2546–2556. [[CrossRef](#)]
3. Schmit, T.J.; Griffith, P.; Gunshor, M.M.; Daniels, J.M.; Goodman, S.J.; Lehair, W.J. A Closer Look at the ABI on the GOES-R Series. *Bull. Am. Meteorol. Soc.* **2017**, *98*, 681–698. [[CrossRef](#)]
4. Okuyama, A.; Andou, A.; Date, K.; Hoasaka, K.; Mori, N.; Murata, H.; Tabata, T.; Takahashi, M.; Yoshino, R.; Bessho, K. Preliminary validation of Himawari-8/AHI navigation and calibration. *Proc. SPIE* **2015**, *9607*, 96072E. [[CrossRef](#)]

5. Kalluri, S.; Alcala, C.; Carr, J.; Griffith, P.; Lehair, W.; Lindsey, D.; Race, R.; Wu, X.; Zierk, S. From Photons to Pixels: Processing Data from the Advanced Baseline Imager. *Remote Sens.* **2018**, *10*, 177. [[CrossRef](#)]
6. Ignatov, A.; Zhou, X.; Petrenko, B.; Liang, X.; Kihai, Y.; Dash, P.; Stroup, J.; Sapper, J.; DiGiacomo, P. AVHRR GAC SST Reanalysis Version 1 (RAN1). *Remote Sens.* **2016**, *8*, 315. [[CrossRef](#)]
7. Kramar, M.; Ignatov, A.; Petrenko, B.; Kihai, Y.; Dash, P. Near real time SST retrievals from Himawari-8 at NOAA using ACSPO system. *Proc. SPIE* **2016**, 9827, 98270L. [[CrossRef](#)]
8. Petrenko, B.; Ignatov, A.; Kramar, M.; Kihai, Y. Exploring new bands in multichannel regression SST algorithms for the next generation infrared sensors at NOAA. *Proc. SPIE* **2016**, 9827, 98270N. [[CrossRef](#)]
9. Liang, X.; Ignatov, A.; Kramar, M.; Yu, F. Preliminary inter-comparison between AH1, VIIRS and MODIS clear-sky radiances for accurate SST retrievals. *Remote Sens.* **2016**, *8*, 203. [[CrossRef](#)]
10. Kawai, Y.; Kawamura, H. Evaluation of the diurnal warming of sea surface temperature using satellite-derived marine meteorological data. *J. Oper. Oceanogr.* **2002**, *58*, 805–814. [[CrossRef](#)]
11. Gentemann, C.L.; Minnett, P.J.; Le Borgne, P.; Merchant, C.J. Multi-satellite measurements of large diurnal warming events. *Geophys. Res. Lett.* **2008**, *35*, L22602. [[CrossRef](#)]
12. Merchant, C.J.; Filipiak, M.J.; Le Borgne, P.; Roquet, H.; Autret, E.; Piolle, J.-F.; Lavender, S. Diurnal warm-layer events in the western Mediterranean and European shelf seas. *Geophys. Res. Lett.* **2008**, *35*, L04601. [[CrossRef](#)]
13. Karagali, I.; Hoyer, J. Characterization and quantification of regional diurnal SST cycles from SEVIRI. *Ocean Sci.* **2014**, *10*, 745–758. [[CrossRef](#)]
14. Donlon, C.J.; Minnett, P.J.; Gentemann, C.; Nightingale, T.J.; Barton, I.J.; Ward, B.; Murray, M.J. Toward improved validation of satellite sea surface skin temperature measurements for climate research. *J. Clim.* **2002**, *15*, 353–369. [[CrossRef](#)]
15. Donlon, C.; Robinson, I.; Casey, K.; Vazquez-Cuervo, J.; Armstrong, E.; Arino, O.; Gentemann, C.; May, D.; LeBorgne, P.; Piollé, J.; et al. The Global Ocean Data Assimilation Experiment High-Resolution Sea Surface Temperature Pilot Project. *BAMS* **2007**, 1197–1213. [[CrossRef](#)]
16. Merchant, C.J.; Harris, A.R.; Roquet, H.; Le Borgne, P. Retrieval characteristics of non-linear sea surface temperature from the Advanced Very High Resolution Radiometer. *Geophys. Res. Lett.* **2009**, *36*, L17604. [[CrossRef](#)]
17. Liang, X.; Ignatov, A.; Kihai, Y. Implementation of the Community Radiative Transfer Model (CRTM) in Advanced Clear-Sky Processor for Oceans (ACSPO) and validation against nighttime AVHRR radiances. *J. Geophys. Res.* **2009**, *114*, D06112. [[CrossRef](#)]
18. Brasnett, B.; Surcel Colan, D. Assimilating retrievals of sea surface temperature from VIIRS and AMSR2. *J. Atmos. Ocean. Technol.* **2016**, *33*, 361–375. [[CrossRef](#)]
19. Global Forecast System. Available online: <https://www.ncdc.noaa.gov/data-access/model-data/model-datasets/global-forecast-system-gfs> (accessed on 18 October 2018).
20. Zhang, H.; Beggs, H.; Merchant, C.J.; Wang, X.H.; Majewski, L.; Kiss, A.E.; Rodríguez, J.; Thorpe, L.; Gentemann, C.; Brunke, M. Comparison of SST diurnal variation models over the tropical warm pool region. *J. Geophys. Res.* **2018**, *123*. [[CrossRef](#)]
21. Karagali, I.; Hoyer, J.; Hasager, C.B. SST diurnal variability in the North Sea and the Baltic Sea. *Remote Sens. Environ.* **2012**, *121*, 159–170. [[CrossRef](#)]
22. Le Borgne, P.; Legendre, G.; Marsouin, A. Operational SST retrieval from MSG/SEVIRI data. In Proceedings of the EUMETSAT Meteorological Satellite Conference, Helsinki, Finland, 12–16 June 2006; Available online: <http://citeseerx.ist.psu.edu/viewdoc/summary?doi=10.1.1.556.9259> (accessed on 19 January 2019).
23. Walton, C.C.; Pichel, W.G.; Sapper, J.F.; May, D.A. The development and operational application of nonlinear algorithms for the measurement of sea surface temperatures with the NOAA polar-orbiting environmental satellites. *J. Geophys. Res.* **1998**, *103*, 27999–28012. [[CrossRef](#)]
24. Merchant, C.J.; Le Borgne, P.; Roquet, H.; Marsouin, A. Sea surface temperature from a geostationary satellite by optimal estimation. *Remote Sens. Environ.* **2009**, *113*, 445–457. [[CrossRef](#)]
25. Petrenko, B.; Ignatov, A.; Kihai, Y.; Stroup, J.; Dash, P. Evaluation and selection of SST regression algorithms for JPSS VIIRS. *J. Geophys. Res.* **2014**, *119*, 4580–4599. [[CrossRef](#)]

26. Rodgers, C.D. Inverse Methods for Atmospheric Sounding: Theory and Practice. 2000. Available online: https://books.google.com.hk/books?hl=zh-TW&lr=&id=FjxqDQAAQBAJ&oi=fnd&pg=PR7&dq=Inverse+Methods+for+Atmospheric+Sounding:+Theory+and+Practice&ots=AR7C7Y3CYo&sig=bnSKbikKEcM_O0_hVmwcxkWyiug&redir_esc=y#v=onepage&q=Inverse%20Methods%20for%20Atmospheric%20Sounding%3A%20Theory%20and%20Practice&f=false (accessed on 19 January 2018).
27. Kurihara, Y.; Murakami, H.; Kachi, M. Sea surface temperature from the new Japanese geostationary meteorological Himawari-8 satellite. *Geophys. Res. Lett.* **2016**. [[CrossRef](#)]
28. Le Borgne, P.; Roquet, H.; Merchant, C.J. Estimation of sea surface temperature from the Spinning Enhanced Visible and Infrared Imager, improved using numerical weather prediction. *Remote Sens. Environ.* **2011**, *115*, 55–65. [[CrossRef](#)]
29. Saux Picard, S. Algorithm Theoretical Basis Document for MSG/SEVIRI Sea Surface Temperature Data Record. Available online: http://www.osi-saf.org/lml/doc/osisaf_cdop3_ss1_atbd_msg_sst_data_record.pdf (accessed on 16 October 2018). [[CrossRef](#)]
30. Petrenko, B.; Ignatov, A.; Shabanov, N.; Kihai, Y. Development and evaluation of SST algorithms for GOES-R ABI using MSG SEVIRI as a proxy. *Remote Sens. Environ.* **2011**, *115*, 3647–3658. [[CrossRef](#)]
31. Merchant, C.J.; Le Borgne, P.; Roquet, H.; Legendre, G. Extended optimal estimation techniques for sea surface temperature from the Spinning Enhanced Visible and Infra-Red Imager (SEVIRI). *Remote Sens. Environ.* **2013**, *131*, 287–297. [[CrossRef](#)]
32. Petrenko, B.; Ignatov, A.; Kihai, Y.; Zhou, X.; Stroup, J. SST algorithms in ACSPO reanalysis of AVHRR GAC data from 2002–2013. *Proc. SPIE* **2014**, *9111*, 91110E. [[CrossRef](#)]
33. Xu, F.; Ignatov, A. In situ SST Quality Monitor (iQuam). *J. Atmos. Ocean. Technol.* **2014**, *31*, 164–180. [[CrossRef](#)]
34. iQuam System. Available online: <https://www.star.nesdis.noaa.gov/sod/sst/iquam/> (accessed on 16 October 2018).
35. Dash, P.; Ignatov, A.; Kihai, Y.; Sapper, J. The SST Quality Monitor (SQUAM). *J. Atmos. Ocean. Technol.* **2010**, *27*, 1899–1917. [[CrossRef](#)]
36. SQUAM System. Available online: <https://www.star.nesdis.noaa.gov/sod/sst/squam/> (accessed on 16 October 2018).
37. Prabhakara, C.; Dalu, G.; Kunde, V.G. Estimation of sea surface temperature from remote sensing in the 11- to 13 μm window region. *J. Geophys. Res.* **1974**, *79*, 5039–5044. [[CrossRef](#)]
38. Aoki, T. On the information content of the satellite measured infrared radiation in the atmospheric window region. *J. Meteorol. Soc. Jpn.* **1979**, *57*, 73–78. [[CrossRef](#)]
39. Petrenko, B.; Ignatov, A.; Kihai, Y.; Heiding, A. Clear-sky mask for the Advanced Clear-Sky Processor for Oceans. *J. Atmos. Ocean. Technol.* **2010**, *27*, 1609–1623. [[CrossRef](#)]
40. Donlon, C.; Martin, M.; Stark, J.; Roberts-Jones, J.; Fiedler, E.; Wimmer, W. The operational sea surface temperature and sea ice analysis (OSTIA) system. *Remote Sens. Environ.* **2012**, *116*, 140–158. [[CrossRef](#)]
41. Reynolds, R.W.; Smith, T.M.; Liu, C.; Chelton, D.B.; Casey, K.S.; Schlax, M.G. Daily high-resolution-blended analyses for sea surface temperature. *J. Clim.* **2007**, *20*, 5473–5496. [[CrossRef](#)]

